Indonesian Geotechnical Journal, August 2026, Vol 5 (2). Page 55-74
DOI: https://doi.org/10.56144/igj.v5i2.155
EISSN: 2829-7520
https://indonesian-geotechnical-journal.org/index.php/JGI/issue/archive

Three-Dimensional Soil-Structure Interaction Analysis of Top-Down Basement Excavation in Jakarta Soft Soil Condition Considering Numerical Instability

Rey Mayo Lais[1,*], Alfred Jonathan Susilo[2,*],
[1]Master Program in Civil Engineering, Faculty of Engineering, Tarumanagara University, Jakarta, Indonesia, 11440;
[2]Department of Civil Engineering, Faculty of Engineering, Tarumanagara University, Jakarta, Indonesia, 11440;
*Correspondence: reymayolais@gmail.com

SUBMITTED 15 May 2026 **REVISED** 18 June 2026 **ACCEPTED** 20 June 2026

ABSTRACT Basement construction in dense urban areas with soft clay deposits requires excavation support system capable of controlling ground deformation and retaining structure responses during staged excavation. This study evaluates the behavior of a top-down excavation system in Jakarta soft clay using three-dimensional finite element modelling with a soil–structure interaction approach. The numerical model was conducted using MIDAS GTS NX and consisted of soil layers, a diaphragm wall, ring slabs, a raft foundation, kingposts, bored piles, and soil–structure interface elements. The soil was modeled using the Hardening Soil Model, while the structural components were modeled as linear elastic elements. Soil parameters were interpreted from borehole data, Standard Penetration Test results, Cone Penetration Test results, and laboratory tests. The results show that the lateral displacement of the diaphragm wall increased with excavation depth due to the release of lateral earth pressure on the excavated side. A fully converged response was obtained up to the Basement 3 excavation stage, with a maximum diaphragm wall displacement of 9.77 mm, corresponding to approximately 0.10% of the excavation depth. The representative vertical displacement section showed a surface settlement of approximately 6 mm and an upward movement of approximately 16 mm at the excavation base, indicating a basal heave tendency without confirmed basal failure. Principal stress and maximum shear stress distributions showed stress concentrations around ring slab elevations, slab openings, and diaphragm wall corners. These results indicate that the ring slabs acted not only as floor elements but also as lateral restraint members that contributed to stress redistribution and wall deformation control. The subsequent excavation stage experienced numerical non-convergence, which was interpreted as a numerical failure or a sign of local instability rather than a confirmed global stability failure. Overall, this study highlights the importance of three-dimensional soil–structure interaction modelling for evaluating top-down excavation behavior in soft clay.

KEYWORDS Top-down excavation; Soil-Structure Interaction; Diaphragm Wall; Ring Slab; Finite Element Analysis

1 INTRODUCTION

Basement construction in dense urban areas such as Jakarta is commonly constrained by limited land availability, adjacent buildings, existing utilities, and soft soil deposits. These conditions may cause significant changes in the initial stress state during excavation, leading to diaphragm wall deformation, ground settlement, stress redistribution within the soil–structure system, as well as potential excavation-induced upward ground movement. The top-down construction method is often adopted for deep basement excavation because ring slabs can function as permanent structural members while simultaneously providing lateral restraint on the diaphragm wall. However, the behavior of this system is complex because the soil, diaphragm wall, ring slabs, groundwater conditions, and staged excavation sequence interact progressively during construction. Recent studies have shown that deep excavation performance in soft clay is strongly influenced by wall stiffness, support stiffness, drainage conditions, construction sequences, and field installation effects (Sandene, et al., 2024; Uribe-Henao, et al., 2023; Zhao, et al., 2024; Xiao, et al., 2023).

Although conventional approaches such as empirical correlations, limit equilibrium methods, and beam-on-spring models are still widely used in practice, these simplified methods may not fully capture the three-dimensional soil–structure interaction response of deep excavations. In addition, conventional design approaches often evaluate geotechnical and structural aspects separately, so the two-way interaction between soil and structural elements during staged excavation may not be fully represented. This limitation becomes more significant in excavations with irregular geometry, corner effects, nonuniform restraint, and staged activation of structural elements. Abbas et al. (2023) showed that excavation shape and corner configuration influence wall deflection and ground settlement, while Li et al. (2022) emphasized that diaphragm wall corner effects can significantly modify the deformation pattern of special-shaped foundation pits. Other recent studies have also demonstrated the importance of three-dimensional numerical analysis for evaluating wall deformation, dewatering-induced settlement, and the influence of neighboring structures on excavation performance (Hsu et al., 2024; Yang et al., 2025; Zhang et al., 2025) These findings indicate that plane-strain or simplified two-dimensional assumptions may be insufficient for evaluating the actual response of deep excavations in complex urban soft soil conditions.

Previous studies on top-down excavation and deep basement systems have provided important insights into construction performance, diaphragm wall behavior, and excavation stability (Parsa-Pajouh et al., 2021; Rodriguez & Beauvilain, 2023; Domínguez & Paniagua, 2024). However, the specific role of ring slabs as permanent lateral restraint elements has not been comprehensively discussed, particularly in terms of their contribution to diaphragm wall restraint, stress redistribution, and three-dimensional interaction in high-plasticity soft clay conditions. Therefore, this study performs a three-dimensional finite element analysis of a top-down excavation system in Jakarta soft soil using MIDAS GTS NX. The analysis evaluates diaphragm wall deformation, principal stress distribution, maximum shear stress, and the contribution of ring slab activation during staged excavation. The novelty of this study lies in the integrated assessment of the diaphragm wall–ring slab–soil system under local soft soil conditions, with particular attention to three-dimensional stress redistribution and deformation mechanisms that may not be captured by conventional simplified approaches.

In addition to evaluating deformation and stress redistribution, this study discusses the occurrence of numerical non-convergence during the later excavation stages as part of the observed excavation response under the adopted modeling assumptions. The numerical results are interpreted within the limitations of the adopted effective-stress approach and are intended to evaluate the deformation and stress response of the integrated soil–structure system rather than to provide a comprehensive assessment of groundwater-induced effects or analytical basal stability.

2 METHODS

This study adopted a quantitative approach based on three-dimensional finite element modelling to evaluate the soil–structure interaction response of a top-down excavation system in Jakarta soft soil. The analysis was performed using MIDAS GTS NX. The numerical model consisted of soil layers, diaphragm walls, ring slabs, and soil–structure interface elements, which were simulated as an integrated system. This modeling approach was adopted to represent the interaction between the soil mass and structural components during staged excavation.

The soil stratification and engineering parameters were interpreted from borehole logs, Standard Penetration Test (SPT) results, Cone Penetration Test (CPT) results, and laboratory test data. The soil was modeled using the Hardening Soil Model. The diaphragm wall and ring slabs were modeled as three-dimensional solid elements with linear elastic material properties, to ensure their stiffness contribution and interaction with the surrounding soil could be represented consistently in the numerical model. The construction sequence was simulated using staged construction analysis by activating the structural components and deactivating the excavated soil elements according to the excavation sequence.

The numerical results were evaluated in terms of diaphragm wall deformations, principal stress distribution, maximum shear stress distribution, and vertical ground movement. These response parameters were selected to assess the contribution of the ring slab system to lateral restraint and to evaluate the stress redistribution mechanism within the integrated soil–diaphragm wall–ring slab interaction system.

2.1 Soil Investigation Data and Soil Stratification

The soil investigation consisted of six boreholes (DB-1 to DB-6) drilled to depths of approximately 80 to 100 m, and seven Cone Penetration Tests (CPTs), namely S-1 to S-7, each with a 2.5-tonne capacity. The soil investigation locations are shown in Figure 1. The soil stratification at the study site was interpreted based on borehole logs, disturbed and undisturbed soil samples, SPT results, CPT results, and laboratory test results. The N_{SPT} values generally indicate relatively soft to stiff soil conditions in the upper layer and stiffer soil layers with increasing depth. Based on the soil type, plasticity characteristics, N_{SPT} values, CPT resistance, and laboratory test results, the subsurface condition was simplified into several representative soil layers for the numerical model. Table 1 presents the interpreted soil stratification and soil properties.

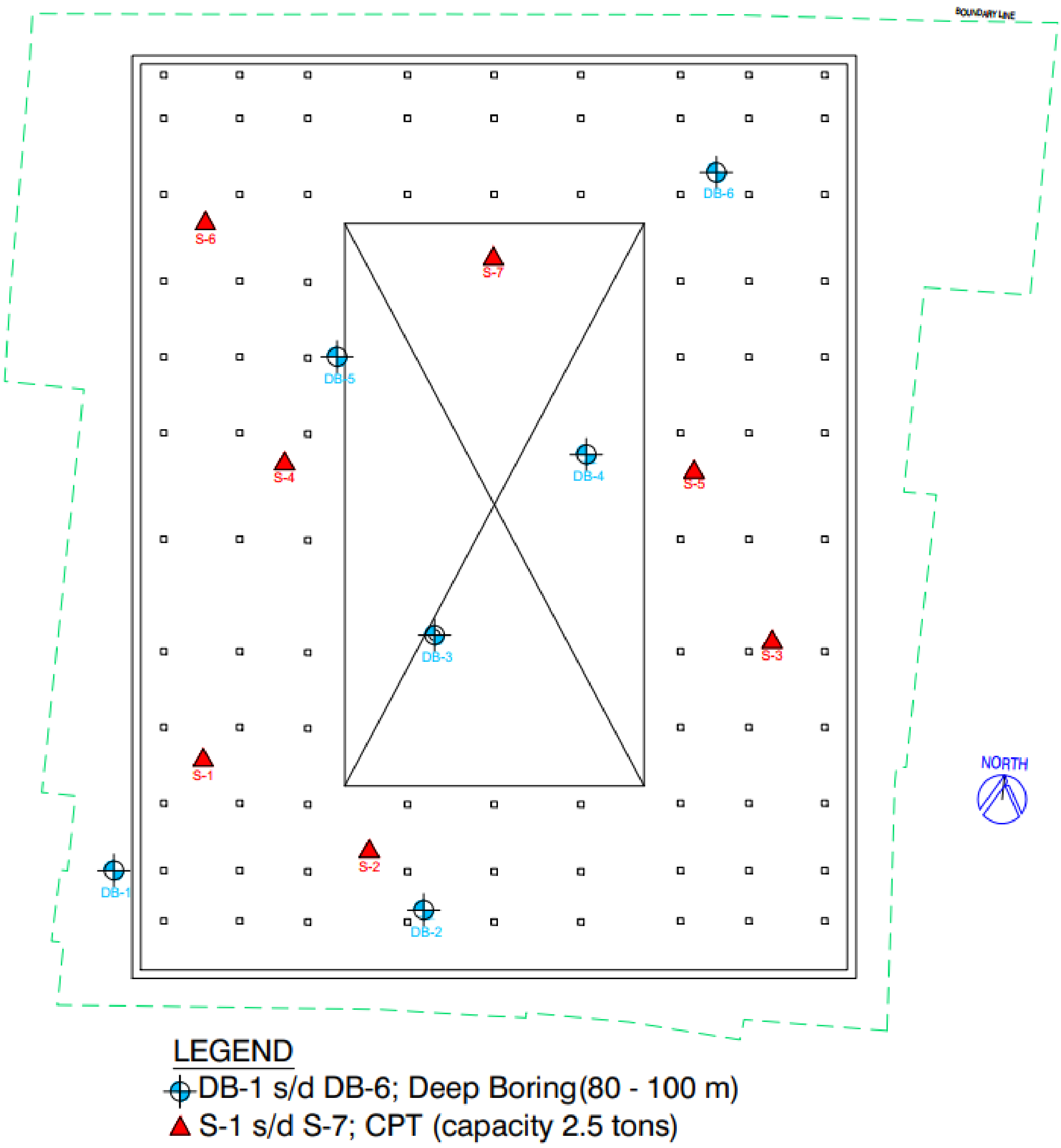

Figure 1. Location map of soil investigation

Table 1. Interpreted soil stratification and soil properties

Depth	Soil type	Soil plasticity	q_c (kg/cm^2)	$\overline{N}_{SPT}$ (blows/ft)
0 – 6 m	High-plasticity silty clay (CH/MH)	LL = 74 PI = 45 wn = 56	5 – 15 (0 – 4 m) 10 – 20 (4 – 5 m) 50 – 250 (5 – 6 m)	4 (range 2 – 9)
6 – 26 m	Sandy silt with interbedded high-plasticity silty clay (ML/SP/SM and CH/MH)		> 250	34 (range 20 – >100)
26 – 35 m	High-plasticity silty clay (CH/MH))	LL = 73 PI = 47 wn = 40		27 (range 17 – 29)
35 – 45 m	Sandy silt and high-plasticity silty clay (ML/SP/SM and CH/MH)	LL = 64 PI = 37 wn = 44		38 (range 21 – 58)
45 – 60 m	High-plasticity silty clay (CH/MH)	LL = 56 PI = 30 wn = 33		29 (range 18 – 45)
60 – 90 m	High-plasticity silty clay (CH/MH)	LL = 72 PI = 44 wn = 33		32 (range 22 – 49)
90 – 100 m	High-plasticity silty clay (CH/MH)	LL = 79 PI = 50 wn = 33		24 (range 18 – 26)

Note: Groundwater level = -2.00 m from ground surface; LL = liquid limit; PI = plasticity index; wn = natural water content; q_c = cone tip resistance; $\overline{N}_{SPT}$ = average SPT value

The groundwater level was identified from the borehole data at approximately −2.00 m below the existing ground surface. This groundwater condition was assigned in the numerical model to generate the initial pore water pressure distribution before the staged excavation analysis was performed. The excavation analysis was conducted using an effective stress approach with the assigned groundwater condition. A fully coupled flow-deformation analysis was not performed; therefore, time-dependent pore water pressure dissipation and consolidation effects were not explicitly considered in the numerical model.

This assumption was considered acceptable for the scope of this study because the analysis focused on the staged mechanical response of the integrated soil–diaphragm wall–ring slab interaction system, particularly wall deformations, stress redistributions, and the contribution of ring slab activation during excavation. Nevertheless, the underlying drainage assumptions were considered when interpreting the results because drainage conditions and pore water pressure dissipation may influence wall movement, ground settlement, and basal heave in soft clay excavations (Uribe-Henao et al., 2023; Sandene et al., 2024). Therefore, the absence of a fully coupled flow-deformation analysis was treated as one of the limitations of this study.

The interpreted soil profile indicated that the upper deposit was dominated by high-plasticity silty clay with relatively low N_{SPT} values, while denser sandy and clayey layers occurred at greater depths. This condition was relevant to deep excavation analysis because the upper clayey deposits may govern excavation-induced deformation and basal stability, whereas the deeper layers influence the embedded response of the diaphragm wall. Previous studies have shown that the behavior of deep excavations in soft clay is affected by soil stiffness, shear strength, drainage condition, support stiffness, groundwater condition, and excavation sequence (Xiao, et al., 2023; Uribe-Henao, et al., 2023; Sandene, et al., 2024).

Considering the excavation depth of 20.5 m, the diaphragm wall tip depth of 35 m, and the model bottom boundary at 40 m below the existing ground surface, the soil profile was simplified into two representative layers: 0–6 m and 6–40 m. This simplification was adopted to reduce model complexity while maintaining the dominant variation of soil strength and stiffness within the excavation influence zone, including the excavation depth, diaphragm wall embedment zone, and surrounding soil mass affecting the numerical response. The upper 0–6 m layer was further divided into 0–2 m and 2–6 m sublayers to account for the groundwater level at 2 m below the ground surface, with different unit weight conditions assigned above and below the groundwater table. Other parameters within this interval were represented by interpreted values corresponding to the dominant high-plasticity silty clay behavior. Meanwhile, the 6–40 m interval, consisting of alternating sandy silt and high-plasticity silty clay with generally stiff to hard behavior, was simplified as a single equivalent engineering layer representing the primary embedded zone influencing the diaphragm wall response and overall soil–structure interaction behavior.

The effective shear strength parameters were determined based on effective stress analysis using Consolidated Undrained (CU) triaxial test results with pore water pressure measurements. The processed CU triaxial test results were plotted in the *p′–q* stress space, as shown in Figure 2 and Figure 3.

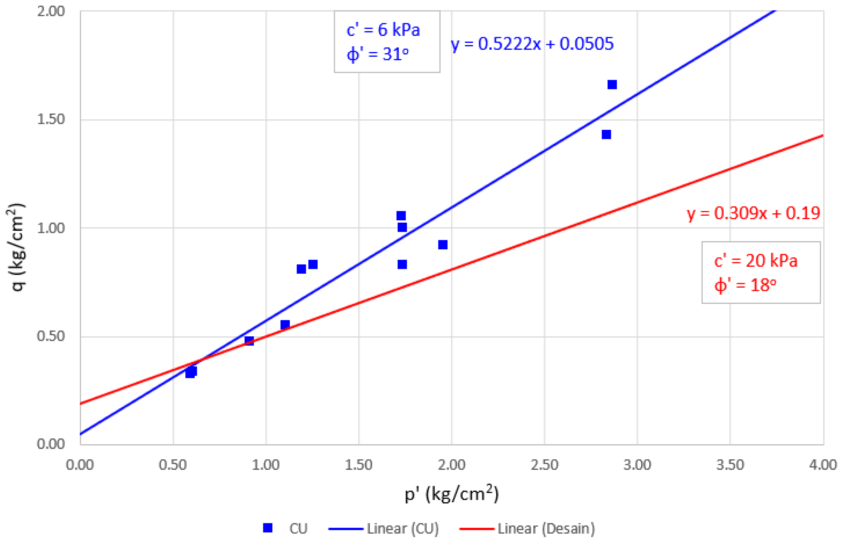

Figure 2. *p′–q* plot of CU triaxial test results in effective stress condition for the 0–6 m depth interval

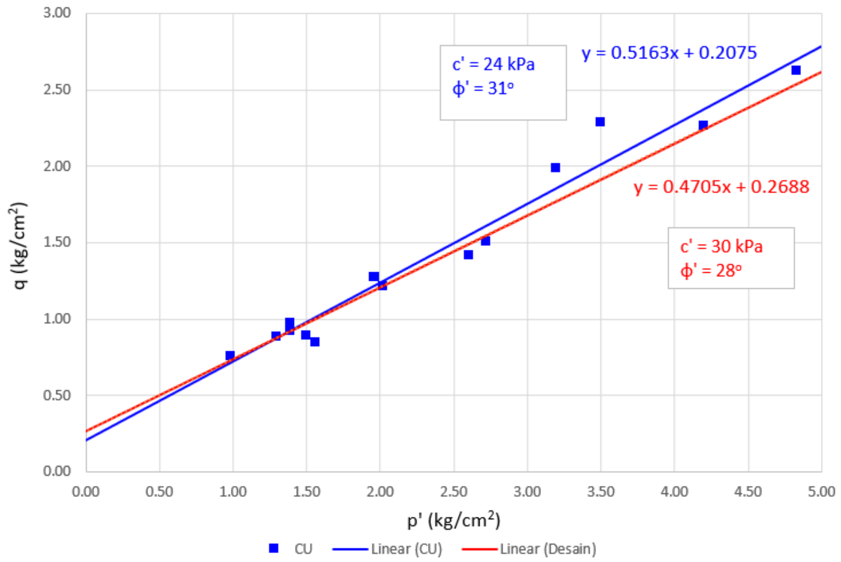

Figure 3. *p′–q* plot of CU triaxial test results in effective stress condition for the 6–40 m depth interval

For the 0–6 m layer, the linear regression of the p'–q plot produced a friction angle of approximately 31°. However, this layer is dominated by high-plasticity silty clay (CH/MH), with high natural water content and plasticity index, as well as a relatively low average N_{SPT} value. Therefore, the regression-based friction angle was considered less representative of the actual mechanical behavior of the upper soft cohesive layer. Consequently, a more conservative design envelope was adopted, resulting in c' = 20 kPa and $\emptyset'$ = 18°, to better reflect the high plasticity, low penetration resistance, and deformation-sensitive behavior of the upper soil layer. For the 6–40 m layer, the regression of the p'–q plot similarly indicated a friction angle of approximately 31°. However, this depth interval consists of non-homogeneous soil deposits, including sandy silt (ML/SP/SM) with interbedded high-plasticity silty clay (CH/MH). Considering the variation in soil type and the presence of fine-grained plastic materials within this interval, a conservative design envelope was also applied. Table 2 summarizes the selected effective shear strength parameters used in the numerical model.

Table 2. Effective shear strength parameters for numerical modeling

Layer	Depth	Representative soil type	c' (kPa)	$\emptyset'$ (°)	Basis for adopted parameters
1	0 – 6 m	High-plasticity silty clay (CH/MH)	20	18	CU triaxial p’-q, CPT, $\bar{N}_{SPT}$, and plasticity. Lower-bound values were adopted to represent the upper soft clay layer
2	6 – 40 m	Sandy silt with interbedded silty clay and high-plasticity silty clay (ML/SP/SM and CH/MH)	30	28	CU triaxial p’-q, CPT, $\bar{N}_{SPT}$, and stratigraphic variation within the excavation influence and D-wall embedment zone

2.2 Soil Constitutive Model Parameters

The soil constitutive model used was the Hardening Soil Model. The Hardening Soil Model was adopted because it can represent non-linear soil behavior for different stiffness parameters for primary loading, one-dimensional compression, and unloading–reloading conditions (Schanz, et al., 1999). Therefore, this model provides a more representative approach for deformation analysis compared with a simple linear elastic or elastic–perfectly plastic model

The main stiffness parameters in the Hardening Soil Model consist of the reference secant stiffness modulus, E_{50}^{ref}, the reference oedometer stiffness modulus E_{oed}^{ref}, and the reference unloading–reloading stiffness modulus E_{ur}^{ref}. The parameter E_{50}^{ref} represents the soil stiffness under triaxial loading, E_{oed}^{ref} represents the stiffness under one-dimensional compression, while E_{ur}^{ref} represents the stiffness during unloading and reloading conditions, which is generally higher than the primary loading stiffness.

For cohesive soils, the undrained shear strength, S_u, was initially interpreted from field penetration data and laboratory testing results to represent the general consistency of the soil layers. However, the stiffness parameters for the Hardening Soil Model were estimated based on the swelling index obtained from oedometer correlations following the approach adopted by Lim et al. (2010), Hsiung et al. (2018) and Li et al. (2023). The reference unloading–reloading stiffness modulus was estimated using Equation (1).

$$E_{ur}^{ref} = \frac{3(1+e_0)p^{ref}(1-2\nu_{ur})}{\kappa} \quad (1)$$

where e_0 is the initial void ratio; ν_{ur} is the unloading/reloading Poisson’s ratio (ν_{ur} is assumed to be 0.2 for clay); p^{ref} is the reference pressure taken as 100 kPa; and $\kappa = C_s/\ln 10$ in which C_s is the swelling index obtained from oedometer testing. For the upper 0–6 m layer, direct consolidation test data were not available; therefore, e_0 was interpreted from the nearest undisturbed samples, while C_s was estimated empirically using the correlations $C_c = 0.009\ (LL - 10)$ and $C_s = 0.2\ C_c$, following the empirical guidance presented by Das and Sobhan (2019).

For sandy or mixed granular soil layers, the stiffness parameters were estimated using the SPT-based approach adopted by Lim et al. (2010), and Li et al. (2023). The Young's modulus was first estimated using Equation (2), in which $E_s = 3000\ N_{SPT}$ was adopted in this study.

$$E_s = (2000{\sim}4000)N_{SPT} \quad \text{[kPa]} \tag{2}$$

The reference unloading–reloading stiffness modulus was then estimated using Equation (3).

$$E_{ur}^{ref} = \frac{E_s}{(\sigma'_3/p^{ref})^m} \tag{3}$$

Where E_s is the Young's modulus, σ'_3 is the minor principal stress, p^{ref} is the reference pressure adopted as 100 kPa, and m is the stress dependency exponent. Values of m = 1.0 and m = 0.5 were adopted for the clayey upper layer and the sandy silt-dominated equivalent lower layer, respectively, following Schanz et al. (1999). The remaining stiffness parameters were estimated following the relationships suggested by Calvello and Finno (2004), as expressed in Equations (4) and (5).

$$E_{50}^{ref} = E_{ur}^{ref}/3 \tag{4}$$

$$E_{oed}^{ref} = 0.7E_{50}^{ref} \tag{5}$$

In addition to stiffness parameters, the Hardening Soil Model also requires effective cohesion, c', effective friction angle, ϕ', dilatancy angle, ψ, failure ratio parameter, R_f, overconsolidation ratio, OCR, and coefficient of earth pressure at rest, K_0. For fine-grained soils such as clay and plastic silt, the dilatancy angle is generally small; therefore ψ = 0° was adopted in this study. For dense granular soils, the dilatancy angle may be estimated as ψ = $\emptyset' - 30°$ as proposed by Bolton (1986). However, for cohesive or mixed fine-grained soils, ψ = 0° is commonly adopted to avoid overestimation of soil strength and stiffness. The failure ratio parameter, R_f, was assigned a value of 0.9 following the commonly recommended value for the Hardening Soil Model (Schanz, et al., 1999). The overconsolidation ratio (OCR) was defined as the ratio between the preconsolidation pressure and the in-situ vertical effective stress. Since site-specific preconsolidation pressure data were unavailable for the simplified soil layers, normally consolidated conditions were assumed for the initial stress generation and OCR = 1.0 was adopted. The coefficient of earth pressure at rest was estimated using Jaky's equation (Jaky, 1944), as expressed in Equation (6),

$$K_0 = 1 - sin\,\emptyset' \tag{6}$$

The upper 0–6 m soil layer was subdivided into two sub-layers (0–2 m and 2–6 m) to account for the groundwater table located approximately 2 m below the existing ground surface. Although both sub-layers were assigned the same strength and stiffness parameters, different unit weights were assigned to represent the unsaturated and saturated soil conditions above and below the groundwater table, respectively. The Hardening Soil parameters used as input in MIDAS GTS NX are summarized in Table 3. The simplified soil layering and corresponding model parameters are illustrated in Figure 4.

The groundwater table was assumed to remain constant at approximately 2 m below the ground surface throughout the analysis. Consequently, the numerical simulations were conducted using an effective-stress approach without considering dewatering processes, transient pore-pressure evolution, or coupled hydro-mechanical interactions. While this assumption enabled a focused evaluation of the excavation-induced soil–structure interaction during staged excavation, it also represents a limitation of the present study Changes in groundwater conditions may influence diaphragm wall deformation, basal heave potential, and ground settlement, particularly in soft clay deposits. Therefore, the predicted responses should be interpreted within the limitations of the adopted groundwater assumption, and future investigations incorporating coupled hydro-mechanical analyses are recommended to capture the effects of groundwater–soil interaction more rigorously.

Table 3. Hardening Soil model parameters

Parameter	Layer 1 (0 – 2 m)	Layer 1 (2 – 6 m)	Layer 2 (6 – 40 m)
γ_{unsat}	16 kN/m^3	16 kN/m^3	17.5 kN/m^3
γ_{sat}	-	16.5 kN/m^3	18 kN/m^3
N_{SPT}	4	4	34
c'	20 kN/m^2	20 kN/m^2	30 kN/m^2
$\emptyset'$	18°	18°	28°
ψ	0°	0°	0°
e_0	1.515	1.515	1.175
C_s	0.058	0.058	0.083
κ	0.025	0.025	0.036
S_u	30 kN/m^2	30 kN/m^2	290 kN/m^2
E_{ur}^{ref}	9,000 kN/m^2	9,000 kN/m^2	100,000 kN/m^2
E_{50}^{ref}	3,000 kN/m^2	3,000 kN/m^2	33,300 kN/m^2
E_{oed}^{ref}	2,100 kN/m^2	2,100 kN/m^2	23,310 kN/m^2
m	1.0	1.0	0.5
K_0	0.69	0.69	0.53

Note: OCR = 1.0; p^{ref} = 100 kN/m^2; R_f = 0.9

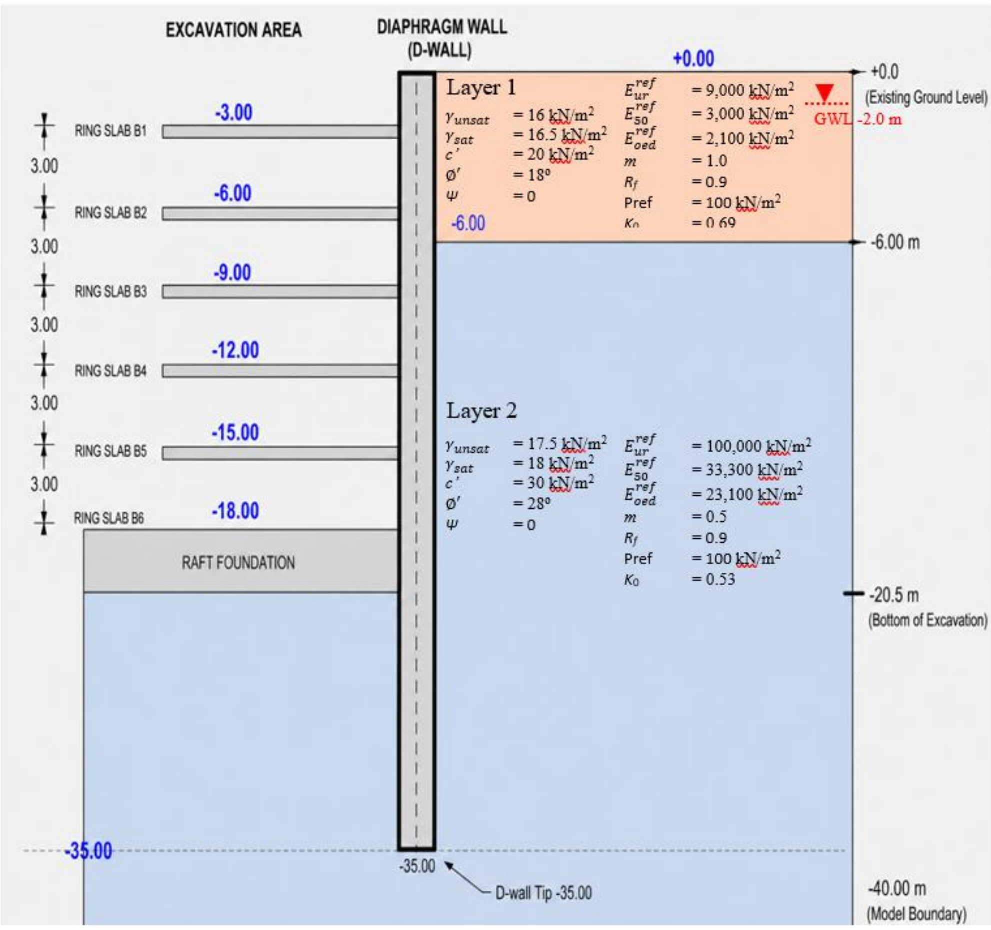

Figure 4. Simplified soil layers and Hardening Soil model parameters used in the numerical model

2.3 Excavation System Modeling on Top-down Construction

The basement geometry was idealized as a rectangular excavation area with a central slab opening. The overall basement plan dimensions were approximately 65.0 m × 83.5 m, with a central opening of approximately 27.5 m × 51.7 m for excavation access, as shown in Figure 5. The basement levels were arranged at 3.0 m vertical intervals, from B1 at −3.0 m to B6 at −18.0 m below the existing ground level, while the final excavation base was located at approximately −20.5 m. The diaphragm wall tip extended to approximately −35.0 m, and the numerical model was extended vertically to approximately −40.0 m to include the excavation base, diaphragm wall embedment zone, and surrounding soil mass influencing the excavation response. The horizontal soil domain was defined sufficiently larger than the excavation area to minimize boundary effects. The ring slab layout, basement elevations, excavation base level, diaphragm wall, and raft foundation position were defined based on the actual construction configuration, as shown in Figure 5 and Figure 6.

The three-dimensional finite element model was developed in MIDAS GTS NX, as shown in Figure 7. The model included the soil domain, diaphragm wall, ring slabs, raft foundation, kingposts, bored piles, and soil–structure interface elements as an integrated soil–structure interaction system. Local mesh refinement was applied around the excavation area, diaphragm wall, ring slab elevations, excavation base, and interface zones to better capture stress redistribution and deformation response during staged excavation.

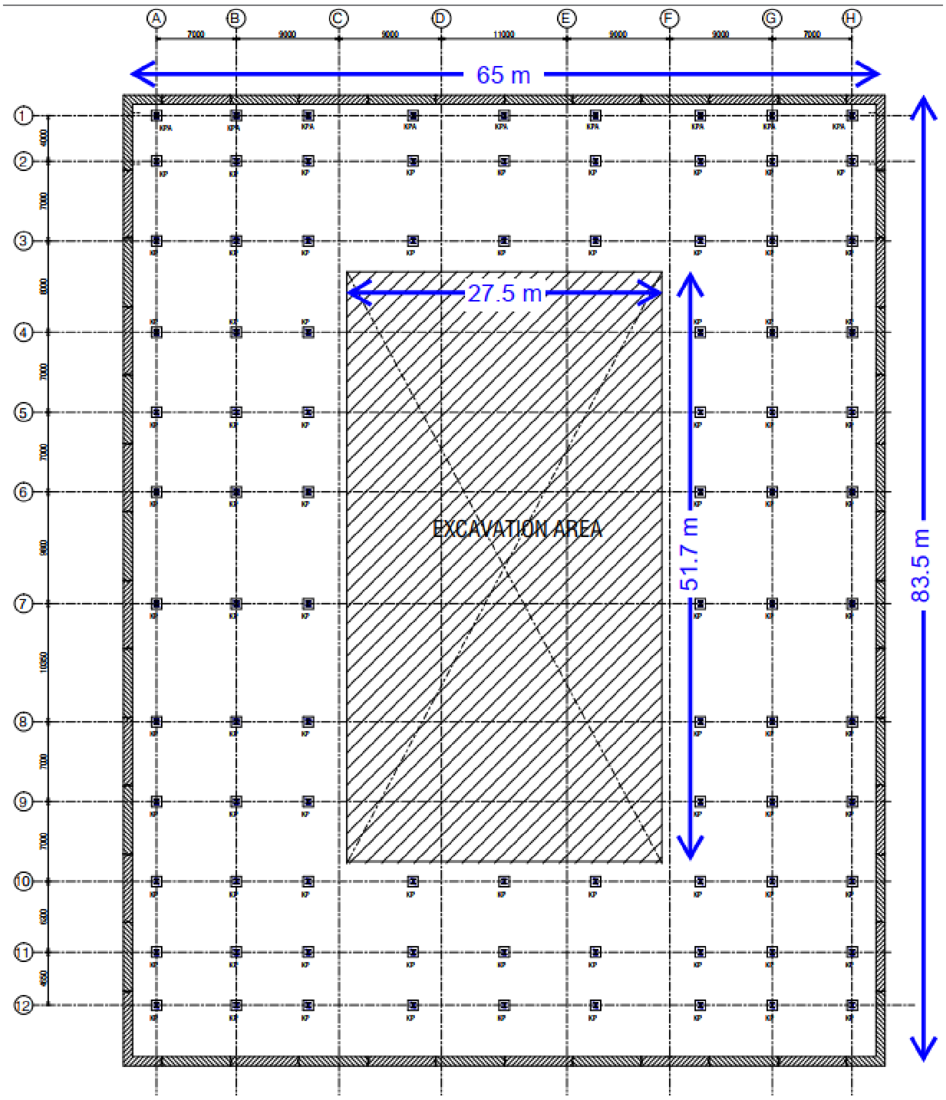

Figure 5. Ring slab layout and central excavation opening

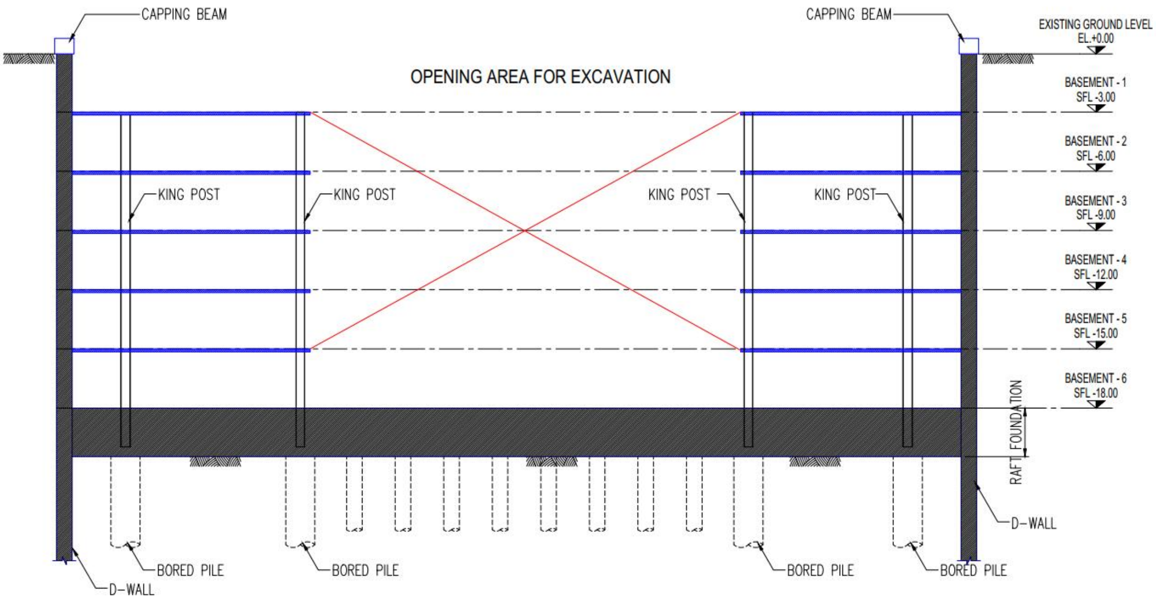

Figure 6. Section of basement excavation and top-down structural system.

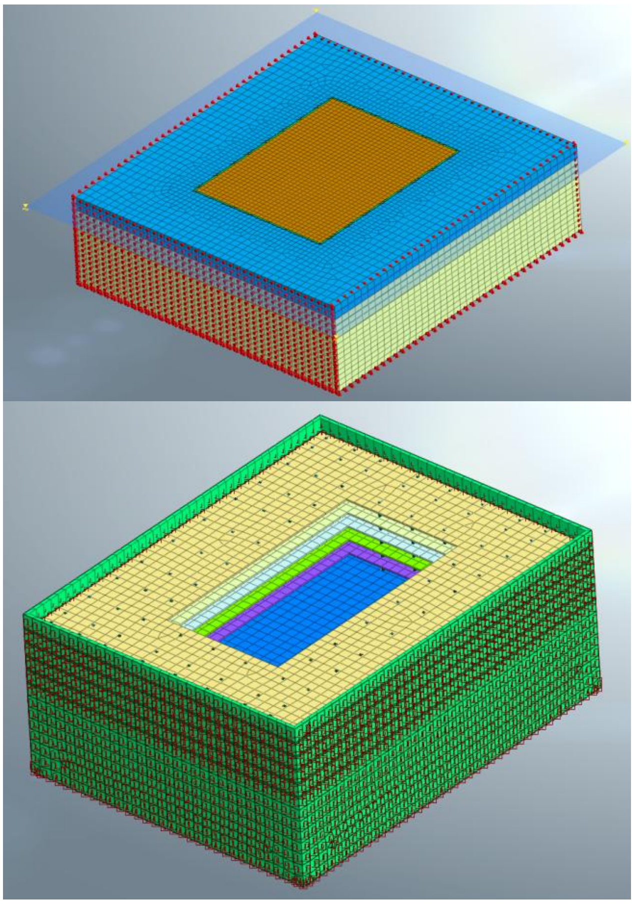

Figure 7. Three-dimensional finite element model of the top-down excavation system in MIDAS GTS NX

The structural elements modeled in the top-down excavation system included the diaphragm wall, ring slabs, kingposts, raft foundation, and bored piles. Each component was defined based on its structural function, stiffness contribution, and role in maintaining excavation stability during staged construction. The diaphragm wall and ring slabs were modeled as three-dimensional solid elements with linear elastic material properties, assuming that the structural components remained within the elastic range throughout the analysis and that no displacement limitation criteria were imposed. The diaphragm wall functioned as the main retaining structure, while the ring slabs provided lateral restraint to the retaining wall during excavation. The ring slabs were assumed to have sufficient structural capacity to remain within the elastic range during the analyzed excavation stages. Therefore, this study does not focus on detailed structural design checks of the ring slabs. The kingposts were modeled as line elements representing temporary steel columns, while the raft foundation and bored piles were modeled to transfer vertical loads to deeper soil layers. The material properties and dimensions of the structural elements used in the numerical model are presented in Table 4 and Table 5.

Table 4. Structural element types and dimensions

Structural Element	**Element type**	**Material model**	**Thickness / Dimension**
D-Wall	3D solid	Linear elastic	0.8 m
Ring slab	3D solid	Linear elastic	0.35 m
Raft foundation	3D solid	Linear elastic	2.5 m
Kingpost	1D line	Linear elastic	H-beam 400x400
Bored Pile	1D line	Linear elastic	Φ 1 m

Table 5. Structural material properties

Structural Element	**Unit Weight (kN/m^3)**	**f_c' (MPa)**	**f_y (MPa)**	**Young's Modulus, E (MPa)**	**Poisson's ratio, ν**
D-Wall	24	30	-	25,742	0.2
Ring slab	24	40	-	29,725	0.2
Raft foundation	24	30	-	25,742	0.2
Kingpost	78	-	250	200,000	0.3
Bored Pile	24	30	-	25,742	0.2

Note: $E_c = 4700\sqrt{f_c'}$ was used for concrete, with E_c and f_c' in MPa, E_s = 200,000 MPa was used for steel.

The soil–structure interaction between the diaphragm wall and the surrounding soil was represented using interface elements. The interface elements were assigned along the contact surfaces between the diaphragm wall and the soil. These elements allowed relative displacement and stress transfer between the soil and structural elements, so the contact behavior was assumed not to be perfectly bonded. This modeling approach was important because wall movement, stress relief, and staged excavation may induce relative shear displacement along the soil–wall interface.

The constitutive behavior of the soil–structure interface was simulated using the Coulomb friction model, with parameters generated via the Interface Material Wizard in MIDAS GTS NX. In this procedure, the interface normal stiffness, shear stiffness, cohesion, and friction angle were computed based on the adjacent soil properties, mesh element size consideration, virtual interface thickness, and strength reduction factor (R_{inter}). Consequently, the values of normal stiffness modulus (K_n) and shear stiffness modulus (K_t) were not independently assumed, but were generated by the software from the stiffness of the adjacent ground elements.

The strength reduction factor was used to reduce the shear strength parameters of the interface relative to the adjacent soil. In this study, R_{inter} = 0.80 was adopted for the soil–diaphragm wall interface. This value was selected because it lies within the recommended range for clay–concrete interfaces and represents a moderate reduction of the soil–wall shear strength to account for imperfect contact between the concrete diaphragm wall and the surrounding clayey soil. The interface strength parameters may be expressed using Equations (6) and (7).

$$c'_{\text{interface}} = R_{\text{inter}}\ c'_{\text{soil}} \quad (6)$$

$$\emptyset'_{\text{interface}} = \tan^{-1}(R_{\text{inter}} \tan\emptyset'_{\text{soil}}) \quad (7)$$

where $c'_{\text{interface}}$ and $\emptyset'_{\text{interface}}$ are the effective cohesion and effective friction angle of the interface, c'_{soil} and $\emptyset'_{\text{soil}}$ are the effective shear strength parameters of the adjacent soil. The soil–structure interface strength parameters were assigned according to the adjacent soil layer properties. For Layer 1, with c' = 20 kPa and $\emptyset'$= 18°, the adopted R_{inter} = 0.80 resulted in $c'_{\text{interface}}$ = 16 kN/m² and $\emptyset'_{\text{interface}}$= 14.6°. For Layer 2, with c' = 30 kN/m² and $\emptyset'$= 28°, the corresponding interface parameters were $c'_{\text{interface}}$ = 24 kN/m² and $\emptyset'_{\text{interface}}$ = 23.04°. This layer-dependent interface assignment was adopted to maintain consistency between the soil shear strength properties and the soil–structure interaction behavior along the diaphragm wall embedment depth. The corresponding normal stiffness modulus (K_n) and shear stiffness modulus (K_t) were automatically calculated by MIDAS GTS NX Interface Material Wizard considering the adjacent soil stiffness, virtual interface thickness, and interface constitutive formulation.

Table 6. Soil-diaphragm wall interface parameters

Parameter	Layer 1	Layer 2
Interface model	Coulomb friction	Coulomb friction
Generation method	MIDAS GTS NX Interface Material Wizard	MIDAS GTS NX Interface Material Wizard
Strength reduction factor, R_{inter}	0.80	0.80
normal stiffness modulus, K_n	731,076.92 kN/m³	706,706.92 kN/m³
shear stiffness modulus, K_t	66,461.54 kN/m³	642,461.54 kN/m³
Interface cohesion, $c'_{\text{interface}}$	16 kN/m²	24 kN/m²
Interface friction angle, $\emptyset'_{\text{interface}}$	14.6°	23.04°
Dilatancy angle, ψ	0°	0°

Note: K_n, K_t, were automatically generated by the MIDAS GTS NX Interface Material Wizard based on the adjacent soil stiffness and interface modelling settings with R_{inter} = 0.80

The soil mass was discretized using three-dimensional solid elements, with size control defined based on element divisions. Local mesh refinement was applied around the excavation area, diaphragm wall, ring slabs, excavation base, and soil–structure interface zones, with an approximate element size of about 2.0 m. A coarser mesh, with an approximate element size of about 3.5–4.0 m, was used in the far-field soil domain to reduce computational cost while maintaining sufficient model accuracy near the excavation system. Boundary conditions were assigned to prevent rigid body movement while allowing realistic ground deformations. The bottom model boundary was fixed in both the horizontal and vertical directions, whereas the lateral boundaries were restrained only in the horizontal direction normal to the boundary and were allowed to move vertically. The ground surface left completely unrestrained to allow vertical and horizontal deformation to occur during excavation. The initial geostatic stress condition was generated using the K_0 procedure prior to initiating the staged excavation analysis.

2.4 Construction Stages in SSI Analysis

The excavation system in this study was analyzed using a staged construction approach to represent the actual sequence of the top-down construction method in the field. This approach captured progressive modifications in geometry, loading conditions, and soil–structure interaction to be simulated during each excavation stage, thereby enabling a realistic evaluation of the system response throughout the entire construction timeline. Staged construction analysis have been shown by Parsa-Pajouh et al. (2021) to yield excellent correlations with field monitoring data for top-down deep excavation systems.

The construction stages adopted in this analysis were described as follows:

a) Stage 0 – Initial condition.
The initial soil stress condition was generated using the K_0 condition.
b) Stage 1 – Installation of diaphragm wall and kingposts
The diaphragm wall and kingpost elements were activated without excavation.
c) Stage 2 – Excavation to the base level of ring slab B1 (-3.35 m)

The soil elements were deactivated to the B1 excavation level, and ring slab B1 was activated as the first lateral support.

d) Stage 3 – Excavation to the base level of ring slab B2 (-6.35 m)
The soil elements were deactivated to the B2 excavation level, and ring slab B2 was activated.

e) Stage 4 – Excavation to the base level of ring slab B3 (-9.35 m)
The soil elements were deactivated to the B3 excavation level, and ring slab B3 was activated.

f) Stage 5 – Excavation to the base level of ring slab B4 (-12.35 m)
The soil elements were deactivated to the B4 excavation level, and ring slab B4 was activated.

g) Stage 6 – Excavation to the base level of ring slab B5 (-15.35 m)
The soil elements were deactivated to the B5 excavation level, and ring slab B5 was activated.

h) Stage 7 – Excavation to the raft foundation level (-20.5 m)
The soil elements were deactivated to the raft foundation level, and the raft foundation was activated as the base structural element.

i) Stage 8 – Final top-down construction condition
The final condition was evaluated after all excavation stages and structural elements had been completed.

2.5 Parameter Evaluation of Excavation System

The numerical results used to evaluate the performance of the excavation system included the lateral deformation of the diaphragm wall, vertical ground movement, principal stress distribution, maximum shear stress distribution, and soil–structure interaction response during the top-down construction simulation. The lateral deformation of the diaphragm wall was evaluated based on the horizontal displacement profile with depth at each construction stage. The maximum lateral displacement was compared with the excavation depth, (H), to evaluate the deformation level of the retaining system. Previous studies have reported that the normalized maximum wall displacement ((\delta_{max}/H)) depends on soil conditions, excavation geometry, support stiffness, groundwater conditions, and construction sequence. Clough & O'Rourke (1990) reported that well-supported braced excavations in soft to medium clay commonly exhibit wall deformation ratios of approximately 0.2–0.5% of the excavation depth. A broader database compiled by Moormann (2004), however, indicated that maximum wall deformation generally ranges from approximately 0.5–1.0% of the excavation depth, with an average value of about 0.87%. These empirical observations were used as reference values to evaluate the relative deformation response predicted by the numerical analysis.

In addition to wall deformations, vertical ground movements were identified to map surface settlements around the excavation area and upward movement at the excavation base. The stress response of the diaphragm wall and ring slabs was evaluated through the distribution of principal stress and maximum shear stress during the staged excavation process. These stress parameters were used to identify stress concentration zones, stress redistribution, and the influence of ring slab activation on the retaining system. The combined evaluation of wall deformation, vertical ground movement, and stress response provided a basis for assessing how the soil, diaphragm wall, ring slabs, and surrounding ground interacted as an integrated excavation support system.

3 RESULTS

The numerical results of the top-down excavation system were obtained from a three-dimensional soil–structure interaction analysis using MIDAS GTS NX. The analysis was initially developed to simulate the excavation sequence up to the raft foundation level. However, a fully converged response was obtained only up to the Basement 3 excavation stage. The subsequent excavation stage remained convergent up to approximately 90% of Excavation Basement 3, after which the analysis log indicated numerical instability during element computations, repeated load bisection, convergence difficulty, and solution divergence. Therefore, the results presented in this section focus on the converged response up to Basement 3, while the subsequent non-convergence is interpreted as a numerical failure or local instability indication rather than a confirmed global stability failure and is further discussed in Section 4.

The maximum wall displacement values obtained from each excavation stage are summarized in Table 7. The results show that the lateral deformation increased with excavation depth due to the release of lateral earth pressure on the excavated side of the diaphragm wall. The maximum lateral displacement increased from 3.80 mm at the Basement 1 excavation stage to 9.77 mm at the Basement 3 stage. When normalized by the excavation depth, the ratio of maximum lateral deformation to excavation depth (δ_{max}/H) remained within approximately 0.10–0.11%. This value is considerably lower than the deformation ranges reported by Clough & O'Rourke (1990) for well-supported braced excavations and substantially lower than the broader database summarized by Moormann (2004). However, relatively small wall displacement ratios have also been reported for excavation systems with high structural stiffness and significant three-dimensional restraint. Hsiung et al. (2018) demonstrated that three-dimensional soil–structure interaction analysis of top-down excavations in Central Jakarta predicted smaller wall deflections than conventional plane-strain conditions due to the contribution of three-dimensional restraint and slab support. Similarly, Hsieh et al. (2019) showed that increasing system stiffness significantly reduced wall displacement in deep excavations constructed in soft clay. Therefore, the relatively small displacement ratio obtained in the present study is considered physically plausible for the converged excavation stages up to Basement 3, although it should not be interpreted as the final excavation response because numerical convergence was not achieved for the subsequent excavation stages.

Table 7. Maximum lateral deformation of the D-Wall

Stage	δ_{max} (mm)	H (m)	δ_{max}/H (%)
B1 Excavation	3.80	3.35	0.11
B2 Excavation	6.07	6.35	0.10
B3 Excavation	9.77	9.35	0.10

Figure 8 presents the lateral displacement of the diaphragm wall during B1, B2, and B3 excavation stages. The displacement profile shows that the wall movement increased as the excavation proceeded. The largest lateral displacement occurred during the B3 excavation stage, with the maximum displacement concentrated around the middle excavation depth. The activation of the ring slabs provided intermediate lateral restraint to the diaphragm wall, as indicated by the change in the displacement profile near the ring slab elevation.

The maximum and minimum principal stress contours at the Basement 3 excavation stage are shown in Figure 9 and Figure 10, respectively. In this study, positive principal stress values were interpreted as tensile stress, while negative values were interpreted as compressive stress. Therefore, the maximum principal stress contour, represented by S-Principal A, indicates the zones where tensile stress concentration developed in the basement structural system. Tensile stress concentration was mainly observed around the ring slab levels, wall corners, and areas affected by stiffness transition between the diaphragm wall and the internal support system. These zones indicate the locations where the structural components experienced local stress redistribution due to lateral restraint and three-dimensional interaction. In contrast, the minimum principal stress contour, represented by S-Principal C, indicates the dominant compressive stress distribution along the diaphragm wall and basement structural system. The compressive stress concentration around the diaphragm wall and corner regions shows that the retaining wall and ring slabs resisted the lateral soil pressure as an integrated support system. The concentration of compressive stress near the corners also indicates that the wall response was affected by three-dimensional boundary effects rather than by uniform plane-strain behavior along the excavation perimeter.

The maximum shear stress contours at the Basement 3 excavation stage are illustrated in Figure 11. The highest shear stress concentration was observed around the ring slab elevations and diaphragm wall corners, and transition zones between the diaphragm wall and the ring slab system. This distribution indicates that the ring slabs participated in transferring lateral forces from the diaphragm wall to the basement structural system. The shear stress concentration near the wall corners and slab opening also reflects the influence of three-dimensional interaction caused by changes in wall direction, slab geometry, and the interaction between adjacent wall panels.

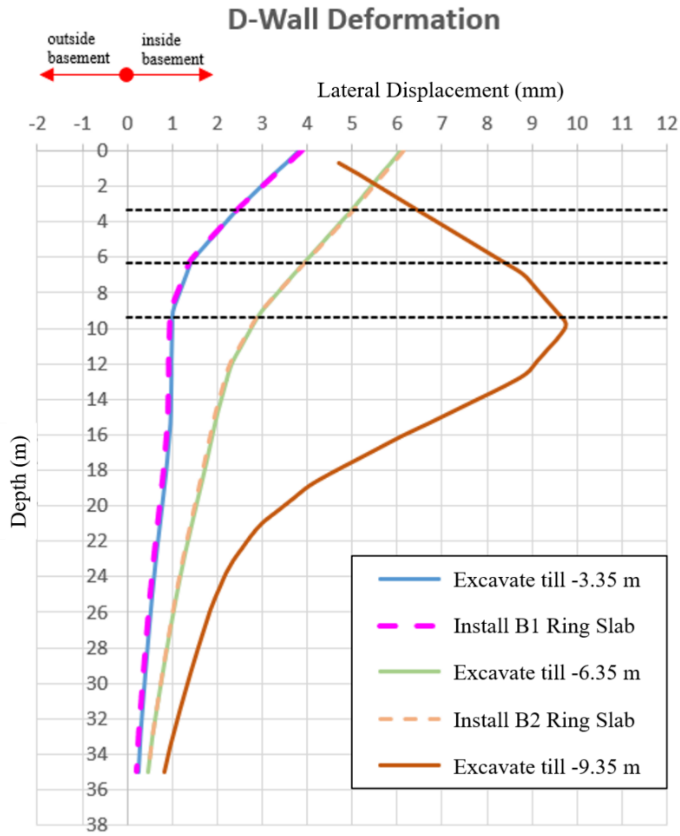

Figure 8. Lateral displacement of the diaphragm wall at B1, B2, and B3 excavation stages.

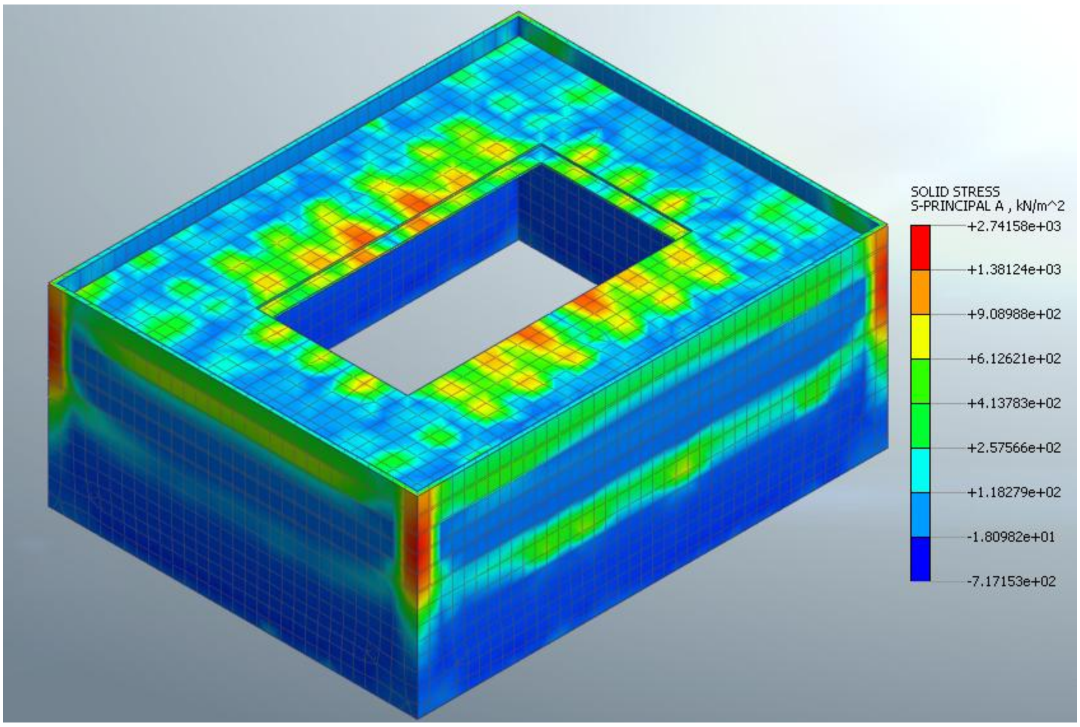

Figure 9. Maximum principal stress contour of the basement structural system, S-Principal A, at the Basement 3 excavation stage, where positive values indicate tensile stress concentration

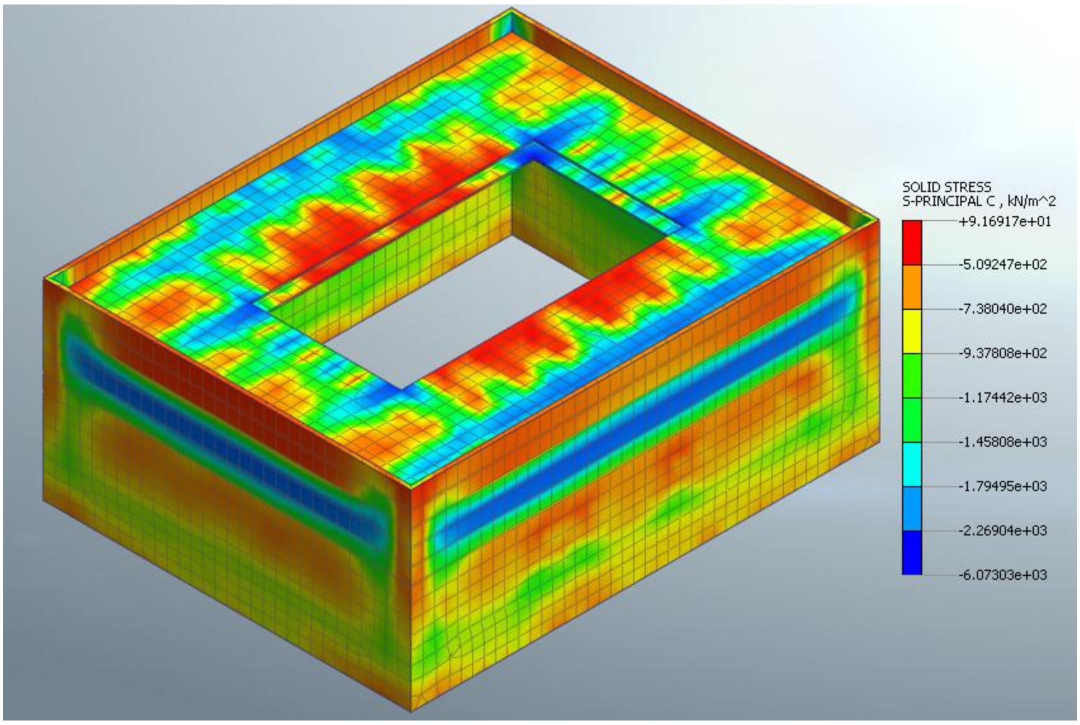

Figure 10. Minimum principal stress contour of the basement structural system, S-Principal C at the Basement 3 excavation stage, where negative values indicate compressive stress concentration

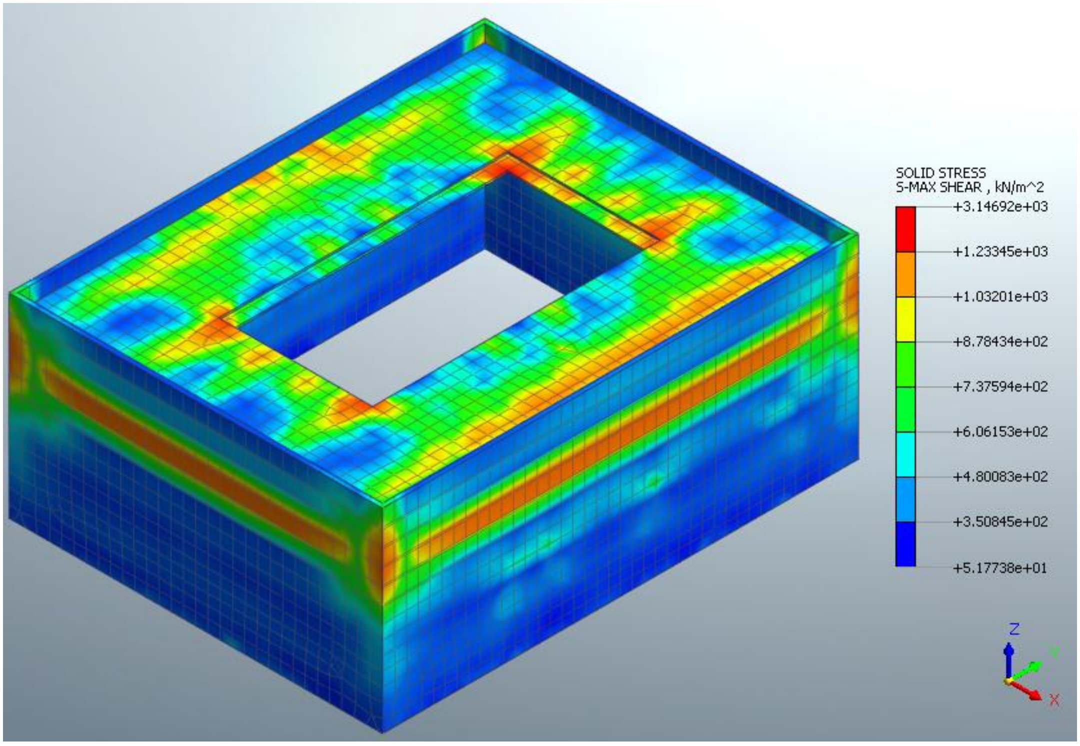

Figure 11. Maximum shear stress contour (S-Max Shear) at the Basement 3 excavation stage

The overall soil–structure interaction response was further evaluated from the vertical displacement pattern of the soil and structural system. Figure 12 illustrates the vertical displacement contours (*Tz*) at the Basement 3 excavation stage where negative *Tz* values indicate downward settlement and positive *Tz* values denote upward movement. The contours reveal that soil movement and structural response developed simultaneously during excavation. The surface settlement around the excavation area was approximately 6 mm, while the upward movement at the excavation base was approximately 16 mm. These values were obtained from the representative section shown in Figure 12. The observed upward movement at the excavation base indicates stress relief within the underlying soft clay caused by excavation. Basal heave assessment using analytical methods such as the Terzaghi, Bjerrum and Eide, or slip-circle method was not conducted in the present study. Therefore, the observed upward displacement should be interpreted as an indication of excavation-induced stress redistribution rather than direct evidence of basal instability.

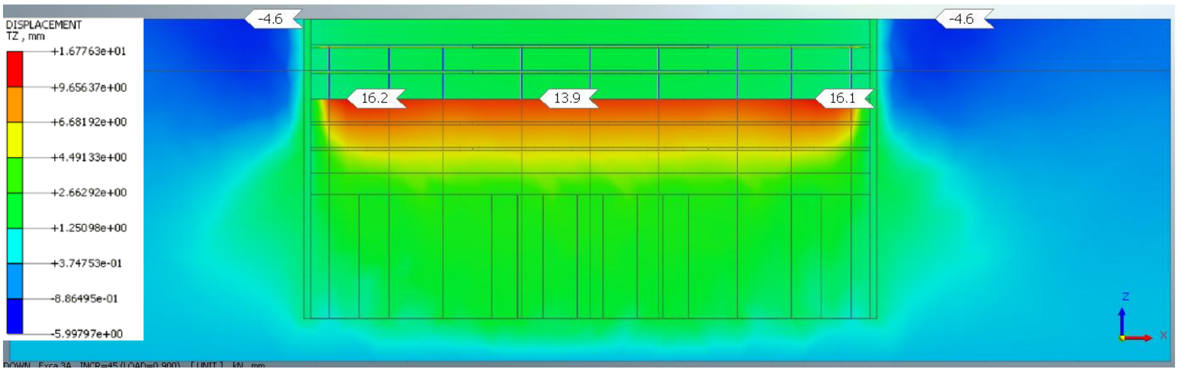

Figure 12. Vertical displacement contour, at the Basement 3 excavation stage

Several numerical improvement measures were attempted during model development, including mesh refinement around the excavation zone, adjustment of interface stiffness parameters, modification of load increment settings, and subdivision of excavation stages. However, numerical convergence beyond the Basement 3 excavation stage still could not be achieved. The model remained converged up to approximately 90% of this stage before numerical instability developed, characterized by repeated load bisection, convergence difficulty, and solution divergence. Therefore, the non-convergence was interpreted as a numerical failure or indication of local instability under the adopted modeling assumptions. Possible contributing factors include localized stress redistribution, progressive soil plasticity, stiffness contrast between the soil and structural elements, soil–wall interface behavior, mesh sensitivity near the excavation and diaphragm wall interface, and local compatibility of the wall–slab connection. Unfortunately, the available converged results were insufficient to conclusively identify a single governing cause, such as local shear failure, excessive mesh distortion, or improper interface behavior.

4 CONCLUSION

The results indicate that three-dimensional soil–structure interaction modeling can provide an integrated interpretation of the deformation and stress response of a top-down excavation system in Jakarta soft clay. The integrated SSI approach provides a more representative evaluation of top-down excavation behavior than a conventional two-stage geotechnical–structural analysis, because the soil layers, diaphragm wall, ring slabs, groundwater condition, interface behavior, and staged construction sequence are modeled simultaneously within one numerical system. This enables the two-way interaction between soil deformation and structural response to be captured more realistically. The diaphragm wall deformation increased with excavation depth up to the Basement 3 stage, with a maximum lateral displacement of 9.77 mm, corresponding to approximately 0.10% of the excavation depth. This value remained below the empirical range generally reported for deep excavations, indicating that the 0.8 m thick diaphragm wall and reinforced concrete ring slabs provided sufficient lateral restraint within the converged excavation stages. The principal stress and maximum shear stress distributions showed stress concentrations around the ring slab elevations, slab opening, and diaphragm wall corners, confirming that the ring slabs contributed not only as floor elements but also as lateral restraint members that transfer horizontal forces, redistribute stresses, and control wall deformation. The vertical displacement pattern showed surface settlement of approximately 6 mm around the excavation area and upward movement of approximately 16 mm at the excavation base in the representative section at Basement 3, indicating a basal heave tendency although basal failure was not directly confirmed. The analysis was limited by non-convergence during the excavation stage toward Basement 3, which was interpreted as a numerical failure or local instability indication rather than a confirmed global stability failure. Possible contributing factors include localized stress redistribution, progressive soil plasticity, stiffness contrast, soil–wall interface behavior, mesh sensitivity, and local compatibility of the wall–slab connection.

DISCLAIMER

The authors declare no conflict of interest.

ACKNOWLEDGMENTS

The author would like to express sincere gratitude to PT Gistama Intisemesta for supporting and providing the data used in this study. The author also gratefully acknowledges Tarumanagara University and PT Midasindo Teknik Utama for their support related to the use of MIDAS GTS NX software. Special appreciation is extended to Mr. Sunarjo Leman for his guidance and assistance in the use of MIDAS GTS NX during the numerical modeling process.

REFERENCES

Abbas, Q., Yoon, J. & Lee, J., 2023. Characterization of Wall Deflection and Ground Settlement for Irregular-Shaped Excavations with Changes in Corner Configuration. *International Journal of Geomechanics,* 23(1), p. 04022258. https://doi.org/10.1061/(ASCE)GM.1943-5622.0002591

Bjerrum, L. & Eide, O., 1956. Stability of strutted excavations in clay. *Géotechnique,* 6(1), pp. 32-47.

Bolton, M. D., 1986. The strength and dilatancy of sands. *Géotechnique,* 36(1), pp. 65-78. https://doi.org/10.1680/geot.1986.36.1.65

Calvello, M. & Finno, R., 2004. Selecting Parameters to Optimize in Model Calibration by Inverse Analysis. *Computers and Geotechnics,* 31(5), pp. 410-424. https://doi.org/10.1016/j.compgeo.2004.03.004

Clough, G. & O'Rourke, T., 1990. Construction induced movements of in situ walls. In: P. Lambe & L. Hansen, eds. *Design and Performance of Earth Retaining Structures.* New York: ASCE, pp. 439-470.

Das, B. M. & Sobhan, K., 2019. *Principles of Geotechnical Engineering.* 9th ed. Boston, MA: Cengage Learning.

Domínguez, R. & Paniagua, W., 2024. Construction, failure and rescue of a diaphragm wall during a deep excavation in Mexico City. *Proceedings of XVII Pan-American Conference on Soil Mechanics and Geotechnical Engineering*.

Hsieh, H., Wang, Z., Lin, T. & Ge, L., 2019. The System Stiffness and Wall Displacement of a Deep Excavation Strengthened with Cross Walls in Soft Clay. *Journal of GeoEngineering,* 14(4), pp. 203-217. https://doi.org/10.6310/jog.201912_14(4).1

Hsiung, B., Yang, K., Aila, W. & Ge, L., 2018. Evaluation of the Wall Deflections of a Deep Excavation in Central Jakarta Using Three-Dimensional Modeling. *Tunnelling and Underground Space Technology,* 72, pp. 84-96. https://doi.org/10.1016/j.tust.2017.11.013

Hsu, C., Tsai, Y., Chen, Y., Li., Y. & Chen, S., 2024. Normalized Analysis of Deformation for Deep Excavation Diaphragm Walls under Different Neighboring Building Conditions. *Results in Engineering,* Volume 22, p. 102155. https://doi.org/10.1016/j.rineng.2024.102155

Jaky, J., 1944. The coefficient of earth pressure at rest. *Journal of the Hungarian Society of Engineers and Architects,* pp. 355-358.

Lim, A., Ou, C. & Hsieh, P., 2010. Evaluation of Clay Constitutive Models for Analysis of Deep Excavation under Undrained Conditions. *Journal of GeoEngineering,* 5(1), pp. 9-20. https://doi.org/10.6310/JOG.2010.5(1).2

Li, Y., Abdi, A., Teng, F. & Ou, C., 2023. Numerical Evaluation on the Application of Small-Strain Stiffness Model for Deep Excavation in Soft Clays. *Journal of GeoEngineering,* 18(3), pp. 121-136. https://doi.org/10.6310/jog.202309_18(3).2

Li, Y., Wang, C., Sun, Y., Wang, R., Shao, G. & Yu, J., 2022. Analysis of Corner Effect of Diaphragm Wall of Special-Shaped Foundation Pit in Complex Stratum. *Frontiers in Earth Science,* 10, p. 794756. https://doi.org/10.3389/feart.2022.794756

Moormann, C., 2004. Analysis of wall and ground movements due to deep excavations in soft soil based on a new worldwide database. *Soils and Foundations,* pp. 87-98. https://doi.org/10.3208/sandf.44.87

Ou, C., 2014. *Deep Excavation: Theory and Practice.* Boca Raton: CRC Press.

Parsa-Pajouh, A., Azari, B., Mirlatifi, S., Buys, H. & Cullen, I., 2021. Numerical analysis of a top-down constructed deep basement with diaphragm walls in Barangaroo, Sydney – A case study. *ISSMGE International Journal of Geoengineering Case Histories,* pp. 95-112. https://doi.org/10.4417/IJGCH-07-01-5

Rodriguez, O. & Beauvilain, A., 2023. Top-down excavation system: An integral solution for challenging deep excavation projects with complex surroundings and difficult geotechnical conditions. *Proceedings of 29th Vancouver Geotechnical Society Symposium Program*.

Sandene, T., Langford, J., Kahlström, M., Long, M., & Ritter, S., 2024. Database for Deep Excavations in Soft Clay with Focus on Groundwater Drainage and Installation Effects. *Journal of Geotechnical and Geoenvironmental Engineering,* 150(11), p. 04024108. https://doi.org/10.1061/JGGEFK.GTENG-12490

Schanz, T., Vermeer, P. A. & Bonnier, P. G., 1999. *The Hardening Soil Model: Formulation and Verification.* s.l., Balkema, pp. 281-296. https://doi.org/10.1201/9781315138206-27

Uribe-Henao, A. F., Arboleda-Monsalve, L. G., Ballesteros, C. & Zapata-Medina, D. G., 2023. Method for Estimating Fully Coupled Response of Deep Excavations in Soft Clays. *Journal of Geotechnical and Geoenvironmental Engineering,* 149(5), p. 04023026. https://doi.org/10.1061/JGGEFK.GTENG-9278

Xiao, Q., Liu, N., Li, M., Chen, J., & Hou, Y., 2023. Performance of a Deep Excavation Supported by Diaphragm Walls Combining with Servo Steel Struts: A Case Study in Hangzhou, China, Soft Clay Deposits. *International Journal of Geomechanics,* 23(12), p. 05023010. https://doi.org/10.1061/IJGNAI.GMENG-8815

Yang, K., Jiang, M., Chi, M. & Feng, G., 2025. Numerical Analysis of Diaphragm Wall Deformation and Surface Settlement Caused by Dewatering and Excavation at Center and End Positions in a Subway Foundation Pit. *Buildings,* 15(15), p. 2796. https://doi.org/10.3390/buildings15152796

Zhang, Z.., Wu, H., Feng, P. & Li, M, 2025. Performance Evaluation for an Adjacent Metro Line Subjected to Ultra-Deep Excavation in Soft Clay: Case Study. *KSCE Journal of Civil Engineering,* Volume 30, p. 100477. https://doi.org/10.1016/j.kscej.2025.100477

Zhao, H., Shen, X., Jia, P. & Zhou, X., 2024. Diaphragm Wall Deformation Behavior and Inclinometer Data Analysis for Braced Deep Excavations. *International Journal of Geomechanics,* 24(6), p. 04024092. https://doi.org/10.1061/IJGNAI.GMENG-8855

- This page is intentionally left blank -